

View Article Online
View Journal

Journal of Materials Chemistry A

Materials for energy and sustainability

Accepted Manuscript

This article can be cited before page numbers have been issued, to do this please use: R. Sharma, A. Rawat, A. Singh, J. M. JOHNY, A. Gautam, J. Parui, T. Das and A. Halder, *J. Mater. Chem. A*, 2025, DOI: 10.1039/D5TA07350B.



This is an Accepted Manuscript, which has been through the Royal Society of Chemistry peer review process and has been accepted for publication.

Accepted Manuscripts are published online shortly after acceptance, before technical editing, formatting and proof reading. Using this free service, authors can make their results available to the community, in citable form, before we publish the edited article. We will replace this Accepted Manuscript with the edited and formatted Advance Article as soon as it is available.

You can find more information about Accepted Manuscripts in the <u>Information for Authors</u>.

Please note that technical editing may introduce minor changes to the text and/or graphics, which may alter content. The journal's standard <u>Terms & Conditions</u> and the <u>Ethical guidelines</u> still apply. In no event shall the Royal Society of Chemistry be held responsible for any errors or omissions in this Accepted Manuscript or any consequences arising from the use of any information it contains.



Fe-Doped CuCo₂S₄ Thiospinel as a High-Performance Oxygen Electrocatalyst for Rechargeable All-Solid-State Zinc-Air Batteries

Ravinder Sharma^c, Abhay Rawat^a, Arkaj Singh^c, Jinta Merlin johny^b, Akriti Gautam^c, Jayanta Parui^b, Tisita Das^a, Aditi Halder^{c*}

^aMaterials Theory for Energy Scavenging (MATES) Lab, Department of Physics, Harish-Chandra Research Institute (HRI), A CI of Homi Bhabha National Institute (HBNI), Chhatnag Road, Jhunsi, Prayagraj 211019, India

^bChemistry Division, School of Advanced Sciences, VIT University, Chennai Campus, Chennai, 600127, India

^cSchool of Chemical Sciences, Indian Institute of Technology Mandi, Himachal Pradesh 175005. *Corresponding author email: aditi@iitmandi.ac.in

Abstract

The commercial viability of rechargeable zinc-air batteries (ZABs) is hindered by their poor round-trip efficiency, dendritic growth of the anode as well as expensive cathode electrocatalysts with limited stability and durability in alkaline medium during prolonged operation. Thus, exploratory researches are essential to replace these platinum-group noble metal catalysts with other stable transition metal oxide. In this work, we demonstrate a facile one-step hydrothermal synthesis of Fe-doped CuCo₂S₄ thiospinels. Both experimental and theoretical analyses confirm that Fe incorporation into the CuCo₂S₄ lattice markedly enhances electrocatalytic activity for ORR and OER compared to the undoped material, by modulating the electronic structure and elevating the metal valence states. The optimized composition, Fe_{0.03}CuCo₂S₄ exhibits outstanding bifunctional activity with an oxygen reduction reaction (ORR) onset potential of 0.89 V vs RHE, a half-wave potential $(E_1/2)$ of 0.80 V vs RHE, and an oxygen evolution reaction (OER) overpotential of 330 mV at 10 mA cm⁻², resulting in a low bifunctional voltage gap (ΔE) of 0.76 V. Furthermore, a prototype ZAB assembled using Fe_{0.03}CCS as the air cathode delivers a peak power density of 82 mW cm⁻² and a specific capacity of 803.4 mAh g_{Zn}⁻¹. The battery demonstrates excellent cycling stability, maintaining performance over 200 cycles (75 hours) at 5 mA cm⁻² with 20-minute charge–discharge intervals. Under depth of discharge study for extended charge—discharge durations (up to 6-hour cycles), the ZAB retains impressive stability for over 50 hours. This study highlights a promising strategy for designing efficient bifunctional electrocatalysts, paving the way for practical applications in next-generation zinc-air batteries.

Introduction

Fossil fuel-based energy systems are largely responsible for the economic expansion, and modernization of growing economies.¹ However, the declining fossil fuel reserves, coupled with the rising global energy demand, poses a serious threat to the long-term sustainability of the global energy supply.² To foster a sustainable energy ecosystem, it is important to utilize the renewable energy resources.³ Unfortunately the intermittent nature of the renewable energy makes it vulnerable for practical application.⁴ Hence to ensure the uninterrupted use of renewable energy, it is important to store it in energy storage devices. This allows users the flexibility and keep a balance between the supply and demand-chain, not restricted with the period of abundance. Therefore, the development of alternative electrochemical energy storage (like Zn-air battery) along with the conversion systems(e.g. fuel cell) builds a sustainable ecosystem to address the energy crisis of the 21st century for sustainable and clean energy technology.⁵⁻⁷

Among many kinds of metal air batteries zinc-air battery withdrew serious attention due to its low cost, environment friendliness and high theoretical energy density (1086 Wh/kg).⁸⁻¹⁰ The operating voltage of zinc air battery is around 1.65 V,¹¹ not a very high voltage for degrading the electrolyte in the aqueous medium. In terms of cost comparison, Li ion batteries cost between \$200 to \$250 per KWh, on the other hand the same for the zinc air batteries cost only \$150. An efficient rechargeable zinc air battery requires a bifunctional electrode material which could efficiently perform oxygen reduction reaction (ORR) during discharging and oxygen evolution reaction (OER) during charging.¹²⁻¹⁴ Unfortunately, both of these processes involve multi-electron with multi-step transfer processes making the reaction kinetics to be sluggish,¹⁵⁻¹⁷ This results into large voltage gap between charging and discharging, lowering the round trip efficiency of 55 to 65%.¹⁸ To lower the cost for the battery and to withdraw a stable energy supply, it is important to develop and design an improved cathode material with good bifunctional activity.

There are many strategies adopted by different research groups to improve the bifunctional activity of the electrode in the rechargeable ZAB.¹⁹⁻²¹ One of the well-adapted strategy to improve the reversible capacity and electrochemical energy storage in battery is through the surface structure engineering and inter-layer spacing expansion.²² Heteroatom insertion in crystal lattice was found to effective in regulating the physicochemical properties of the electrode materials at atomic level.^{23, 24} Recently, ternary thiospinel (AB₂S₄)^{25, 26} materials have gained wider attention

as an oxygen bifunctional electrocatalyst. Thiospinels are having two metal ions (A²⁺ and B³⁺) occupied at a tetrahedral site and an octahedral position with a sulfur atom in a closely packed crystal structure, respectively.²⁷ Such a structure with many redox centers can offer low-energy electron hopping between various metal cations, improving electrical conductivity and providing a large number of active sites for oxygen species adsorption and desorption.²⁸

In this work, we explored a spinel chalcogenide (CuCo₂S₄) as a bifunctional cathode material for zinc-air batteries. We systematically introduced Fe as a dopant into the spinel lattice without disrupting its original crystal structure. The atomic radii of Fe and Co are very similar (125 pm and 126 pm, respectively), and the comparable size facilitates the substitution of Fe³⁺ for Co³⁺ within the CuCo₂S₄ framework. This incorporation leads to a slight lattice expansion and improves the electrochemical reaction kinetics by optimizing the electronic structure and active-site configuration. Lattice strain, both compressive and tensile, can tune the intermediate binding strength and modulate the electronic configuration of transition-metal cations, which consequently enhances the catalytic activity. The similar observation was also noted here. The undoped CuCo₂S₄ shows excellent bifunctional activity with the half wave potential of 0.76V for ORR and overpotential of 370 mV @ 10mA/cm² for OER leading to bifunctional activity (ΔE) of 0.84V, which is capable to produce a power density of 52 mW cm⁻² and specific capacity of 748.8 mAhg_{7n} 1. Systematic doping of Fe in CuCo₂S₄ improves the bifunctional activity where positive half wave potential of 0.80V for ORR and overpotential of 330 mV @ 10mA cm⁻² for OER leading to bifunctional activity of 0.76V, leads to the maximum power density of 82 mW cm⁻² and with specific capacity of 803.4 mAhg_{Zn}⁻¹. The maximum round trip efficiency is found to be 61.72%. The optimization of the dopant Fe in the spinel chalcogenide is crucial. Our experimental data show excessive Fe doping leads to the failure of the performance and phase segregation. Thus, systematic and calculated doping of Fe in CuCo₂S₄ is important to improve its battery performance and rechargeability. Theoretical DFT calculation also reveals that the overpotential values had been decreased significantly on the doped surface and Co site turns out to be the best possible active site with lowest overpotential among all the considered active sites. Substitutional doping modifies the local electronic structure and directly influences electron transfer between the surface and adsorbates, thereby facilitating the OER process, improving the bi-functional activity.

Experimental Section

Chemical & Materials

Cobalt (II) acetate tetrahydrate [Co(CH₃COO)₂.4H₂O, 99%] and ethylene diamine (EDA) (99.5%) were purchased from SRL chemicals. Cupric acetate monohydrate [Cu(CH₃COO)₂.H₂O, 99.0%], pure Sulphur powder and KOH were purchased from Loba Chemicals. Iron (III) Chloride hexahydrate [FeCl₃.6H₂O] was purched from Himedia while Pt/C and RuO₂ were purchased from Alfa Aesar and Sigma Aldrich respectively. Nafion 5 wt% solution was purchased from Metnmat Innovations. All chemicals were used without further purification.

Synthesis of pure Copper Cobalt Sulfide (CCS)

Briefly, to synthesize copper cobalt sulfide (CCS) 1 mmol of copper acetate (0.1996 g) and 2 mmol of cobalt acetate (0.4982 g) were dissolved in 30 mL of deionized water under vigorous stirring for 10 minutes to form a homogeneous solution. In a separate beaker S-EDA complex was prepared by adding 4 mmol of sulphur powder in 3 mL of ethylene diamine. The deep red complex was then added dropwise to the homogeneous solution of copper and cobalt acetate with constant stirring to form a dark brown solution. The dark brown solution was transferred to a Teflon-lined hydrothermal and heated to 180°C for 12h in an oven. After 12h, the hydrothermal was allowed to cool down naturally to room temperature, the black precipitate was then collected through centrifugation and washed several times with DI and ethanol. The collected sample was dried in an oven at 50°C. The synthesis scheme is given in Figure 2(a).

Synthesis of Fe doped samples Fe_xCCS:

The Fe-doped samples were synthesized following the same procedure, with varying amounts of FeCl₃·6H₂O added to the copper acetate and cobalt acetate precursor solution, followed by the dropwise addition of the S–EDA complex and subsequent hydrothermal reaction. The elemental composition of the Fe_xCuCo₂S₄ samples has been quantified using inductively coupled plasma mass spectrometry (ICP–MS). The obtained Fe, Cu, and Co ratios are confirming the successful incorporation of Fe into the CuCo₂S₄ Table S1.

This article is licensed under a Creative Commons Attribution-NonCommercial 3.0 Unported Licence

Access Article. Published on 18 Tachwedd 2025. Downloaded on 19/11/2025 05:45:50.

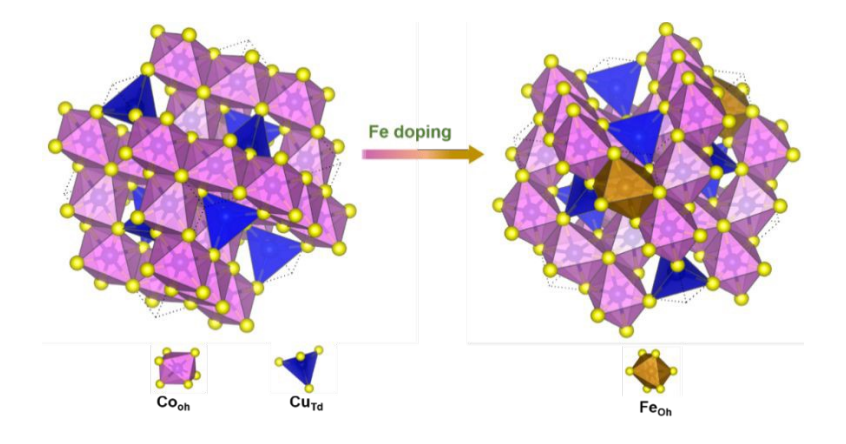


Figure 1 Schematic representation of the crystal structure.

Physical Characterisation

The crystal structure examination were done with the help of Rigaku MiniFlex. The diffraction were recorded from 2θ range 10 to 85° in one degree scan rate with Cu K α radiation (λ =0.154 nm). Raman spectra were recorded using LabRAM HR evolution, Horiba Jobin Vyon, with 532 nm laser. The morphologic analysis of the catalyst was done with the field-emission scanning electron microscope (FE-SEM) facility (Nova Nano SEM 450). Further the high resolutiom transmission electron microscopy (HRTEM) was performed using Tecnai G2 20 S-TWIN TEM having acceleration voltage of 200 KV employing LaB₆ as electron source. The surface analysis and chemical composition of the catalyst were performed by X-ray photoelectron spectroscopy using ThermoFisher Scientific Nexsa, employing Al- K α (λ =1486.6 eV). All the binding energies were calibrated by C1s peak at 284.8eV.

Electrochemical Characterisation

OER studies All electrochemical studies were performed with a conventional three-electrode assembly in a single compartment cell wherein glassy carbon (GCE, Ø 5 mm) containing drop-coated catalyst acted as the working electrode (WE), Pt wire as the counter electrode, and Ag/AgCl (3M KCl) as the reference electrode. The electrochemical measurement was done with the help of electrochemical workstation (Autolab, Metrohm), in N_2 -purged 1M KOH solution as electrolyte. Before each analysis, the GCE was cleaned with alumina slurry of different grits (1, 0.3 and 0.1 µm grain sizes, respectively) and washed with deionized water. Electrochemical impedance spectroscopy (EIS) measurement was performed in the frequency range of 1 MHz to

0.1 Hz. To prepare the working electrode for electrochemical measurements, 3 mg of powder catalyst, mixed with 3mg of Vulcan carbon was dispersed in a blend of deionized water and isopropyl alcohol (2:1) containing 15µl of nafion solution (5 wt%) as a binder and it was ultrasonicated for 30-40 min to form a homogeneous catalyst ink. The loading of the catalyst-ink on GCE was kept as 99.6 µg/cm². All the potentials are referred to RHE for convenience, and current density was normalized by dividing the obtained current with the geometric area of the electrode.

ORR studies: To evaluate the ORR activity of the synthesized catalyst, hydrodynamic experiments, namely rotating disk electrode (RDE) and rotating ring-disk electrode (RRDE) measurements, were performed in 0.1 M KOH. The experiments were performed at various rotation rates between 225 and 2025 rpm at a scan rate of 5 mV s⁻¹ in a three-electrode assembly using a glassy carbon disk-Au ring (Ø 5.5 mm) ring-disk electrode from Pine Research Instrument Inc., USA, as a WE with (10 μL (200 μg/cm²)) of catalyst slurry drop coated on the GCE disk. The measurements were performed both under an inert atmosphere (purged with N₂) and in an oxygen (O₂) saturated media by bubbling it through the electrolyte for 30 min before the start of the experiment and then a constant flow was maintained above the electrolyte throughout the measurements.

Rechargeable Aqueous Zinc-air battery

For practical application, the aqueous rechargeable ZAB was assembled in a two-electrode setup. The cathode part was designed by a porous carbon paper (1 cm x 1 cm) as support coated with catalyst ink. The catalyst ink was prepared by dispersion of 5mg of catalyst with 10mg of Vulcan carbon in a mixture of IPA (485 µl) and DI (485 µl) with the addition of 30 µl Nafion solution (5wt%). Then the 150 μl of catalyst ink was drop-cast over a carbon paper in 1 cm x 1 cm area. The polished Zn foil of the same area was used as an anode. The electrolyte used for the aqueous ZAB testing was 6 M KOH with 0.2 M Zn(acetate)₂.

Rechargeable Solid-State Zinc-air battery

Further, Fe_{0.03}CCS catalysts were also used in solid-state zinc-air batteries to explore for its wider applications. Cathode was made using the conductive carbon cloth as the substrate over which 200 μl of ink containing active catalyst was drop-casted over 1 sq. cm² area of the carbon cloth with the loading of 1 mg cm⁻². PVA KOH membrane was used as the active solid-state electrolyte, which was prepared by using 1.5 g of PVA in 12 ml of water at 80 °C till the solution became viscous. Then, 3ml 9M KOH was added to the solution with constant stirring. Then the solution is poured into the glass petri dish for drying. After drying, the PVA KOH membrane is dipped in 6M KOH for further saturation of electrolyte in the membrane. Further, the above membrane was sandwiched between the cathode and zinc anode to make the solid-state battery.

Result & Discussion

Un-doped $CuCo_2S_4$ is of a spinel phase with the space group of Fd_3m . The thiospinel $CuCo_2S_4$, having the general formula AB_2S_4 , is composed of trivalent Co^{3+} ions occupying octahedral B sites and divalent Cu^{2+} ions present at the tetrahedral A site. The crystalline structure of the synthesized catalyst was examined using the powder X-ray diffraction technique and confirms the crystal structure. The XRD pattern of CCS shows the diffraction peak at 16.69° , 27.11° , 31.78° , 38.46° , 46.76° , 50.50° , 55.28° , 64.91° , 69.12° , 77.85° , and 81.70° which are indexed to the planes (111), (022), (113), (004), (224), (115), (044), (335), (444), (137) and (008) respectively Figure 2(b). The XRD pattern of CCS well matched with the carrollite structure $CuCo_2S_4$ (JCPDS No. 42-1450). The XRD pattern of CCS also consist of some other peaks at 27.7° , 32.2° and 46.2° which are matched with the $Cu_{2-x}S$ (JCPDS No. 00-002-1281). The introduction of Fe in the CCS structure shifts the diffraction peaks towards a slightly lower angle than pristine CCS. This suggests that Fe^{3+} ions have been assimilated into the octahedral Co^{3+} sites. A greater interplanar distance was resulted from the slightly increased ionic radius of Fe^{3+} , leading to a shift of the XRD peak to a lower 2-theta value, in accordance with Bragg's law.

Rietveld refinement of $CuCo_2S_4$ and Fe-doped $CuCo_2S_4$

The XRD patterns of $CuCo_2S_4$ and Fe-doped $CuCo_2S_4$ have been analyzed by multiphase Rietveld refinements with the Fullprof program, employing the Pseudo-Voigt –Axial divergence asymmetry function. The cubic structure with the Fd-3m space group was successfully refined for all peaks of $CuCo_2S_4$ and Fe-doped $CuCo_2S_4$. Less than 6% Cu_2S (Fd₃m) was quantified in $CuCo_2S_4$ and Fe doped $CuCo_2S_4$ as shown in Figure (S1). Fe_{0.01}CCS doping resulted in 97% $CuCo_2S_4$ and 3% Cu_2S . The FeS phase (P63/mmc) was observed to segregate as the Fe doping

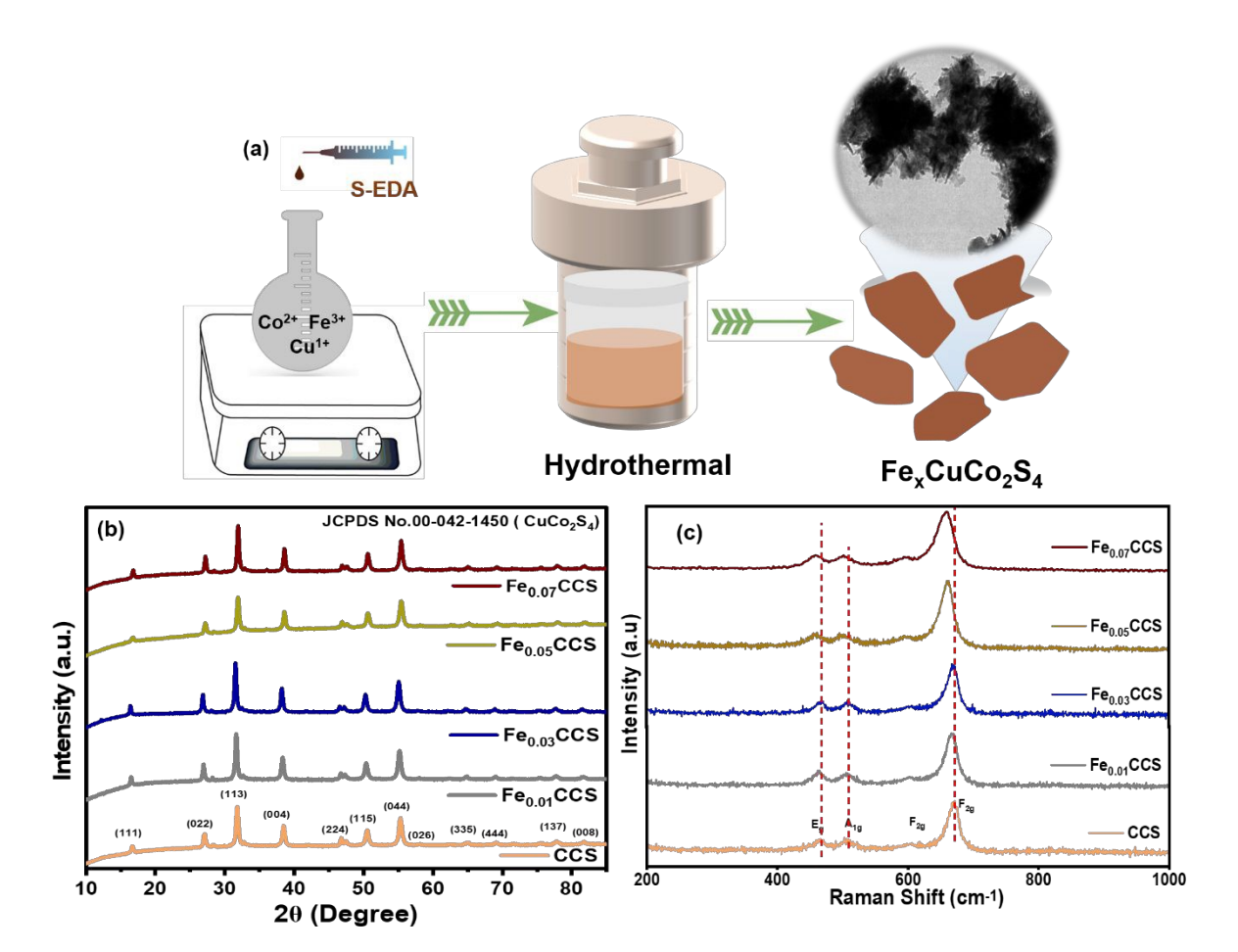


Figure 2 (a) The schematic diagram for the synthesis of Fe_xCuCo₂S₄ (b) XRD patterns of CuCo₂S₄ and $Fe_xCuCo_2S_4$ (X = 0.01, 0.03, 0.05 and 0.07) (c) Raman spectra of $CuCo_2S_4$ and $Fe_xCuCo_2S_4$ (X = 0.01, 0.03, 0.05 and 0.07).

increased leading to a quantification of less than 5%. A slight decrease in unit cell dimension is observed from CuCo₂S₄ (9.47A° Å) to Fe_{0.01}CCS -doped CuCo₂S₄ (9.46 A°) Table S2. This decrease is attributed to the occupancy of Fe in the octahedral site. Further, addition of Fe increases the phase segregation, leads to the formation of FeS, resulting in less occupancy of Fe in the octahedral site of CuCo₂S₄. The Fe_{0.01}CCS and Fe_{0.03}CCS exhibit a negative shift in 2-theta (shift to lower 2-theta) for the (224), (044), and (117) planes. This suggests that Fe³⁺ ions have been assimilated into the octahedral Co³⁺ sites. A greater interplanar distance was resulted from the slightly increased ionic radius of Fe³⁺, leading to a shift of the XRD peak to a lower 2-theta value, in accordance with Bragg's law. With the exception of one plane (224), where there is no 2-theta shift and a lower 2-theta shift is seen in Fe_{0.05}CCS and Fe_{0.07}CCS respectively, a shift to higher 2theta is observed in both of them. (Table S3 in supporting information)

The intensity of the (111) plane is given as 16.63 for the standard JCPDS 042-1450 and is decreased to 16.24 for the pure $CuCo_2S_4$, according to the intensity value of 100 of the (113) plane. The percentage change in relative intensity is displayed in Table S4, where a decrease in intensity is indicated by a negative sign and an increase in intensity relative to the standard JCPDS is indicated by a positive sign. An increase in peak intensity is shown by the (135) & (117) planes of pure $CuCo_2S_4$ and $Fe_{0.03}CCS$, the (117) plane of $Fe_{0.01}CCS$, the (111) & (117) planes of $Fe_{0.05}CCS$, and the (111), (044), (135), & (117) planes of $Fe_{0.07}CCS$. The increased intensity suggests that doped Fe^{3+} may exist in the interstitial voids. The peaks that show a decrease in intensity can be attributed to the inclusion of Fe^{3+} in the octahedral site of Co^{3+} as a slightly weaker scattering effect is produced by it compared to Co^{3+} . The decrease in peak intensity may also be caused by the sulphur point defects. The surrounding metal cations $(Co^{3+}$ & Cu^{2+}) capture the trapped electrons from the sulphur vacancies, reducing Co^{3+} to Co^{2+} and Cu^{2+} to Cu^{+} . This reduction causes an increase in d-spacing due to the larger ionic radius of Co^{2+} & Cu^{+} than Co^{3+} & Cu^{2+} respectively and results in negative 2-theta shifts in XRD.

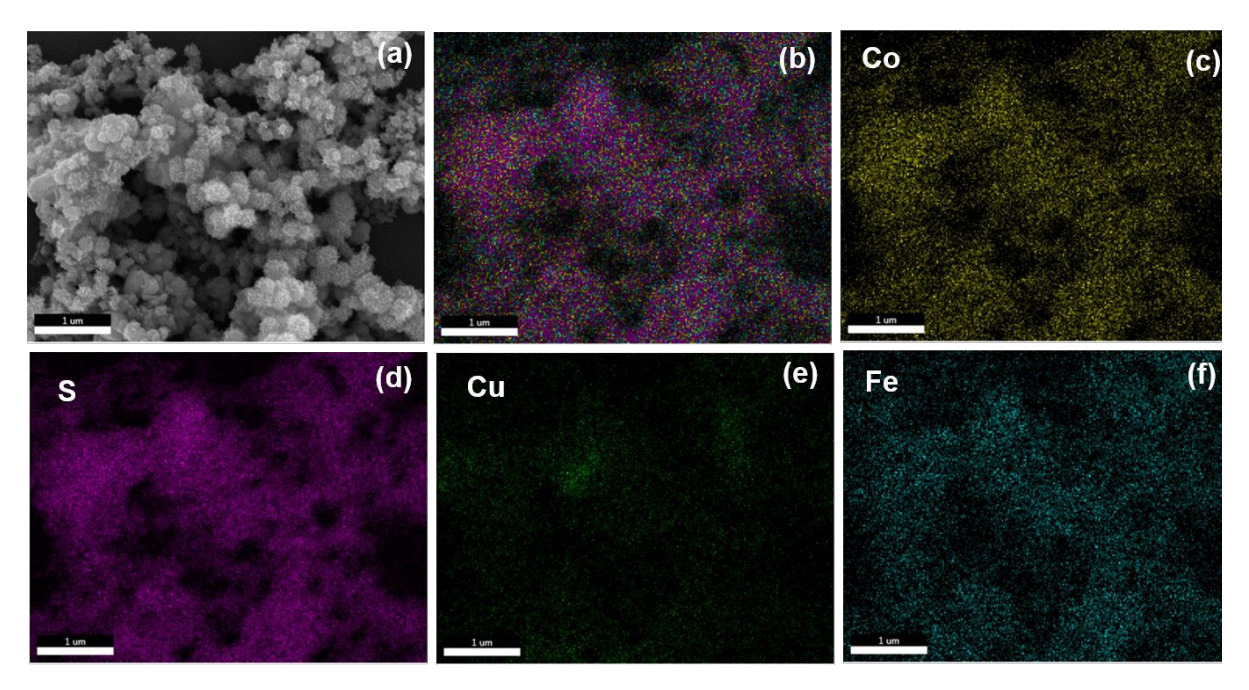


Figure 3: FESEM images at $1\mu m$ (a) Fe_{0.03}CCS (b) SEM EDS mapping of Fe_{0.03}CuCo₂S₄ (c) Co (d) S (e) Cu and (f) Fe.

The chemical nature of the samples was further investigated using Raman spectroscopy. Figure 2(c) shows the Raman spectra for un-doped $CuCo_2S_4$ and the peak observed at 463.7, 503.9 and 601.6 cm⁻¹ are corresponding to E_g , A_{1g} and F_{2g} mode of Co-S bond.²⁵ While the peak observed at

The morphology of the synthesized catalyst was studied by field emission scanning electron microscopy (FESEM). The FESEM images of pure CCS show a nanosheet type of morphology (Figure S2). These nanosheets are not interconnected to each other, and some nanosheets are found flat on the substrate. The Fe doping in the pristine structure has no effect on the morphology (Figure 3(a) and Figure S2). The morphology with the Fe addition remains same. Figure 3(b) shows the EDS mapping of Fe_{0.03}CCS demonstrates the homogeneous distribution of different elements Co, Cu, S and Fe.

This article is licensed under a Creative Commons Attribution-NonCommercial 3.0 Unported Licence

Open Access Article. Published on 18 Tachwedd 2025. Downloaded on 19/11/2025 05:45:50.

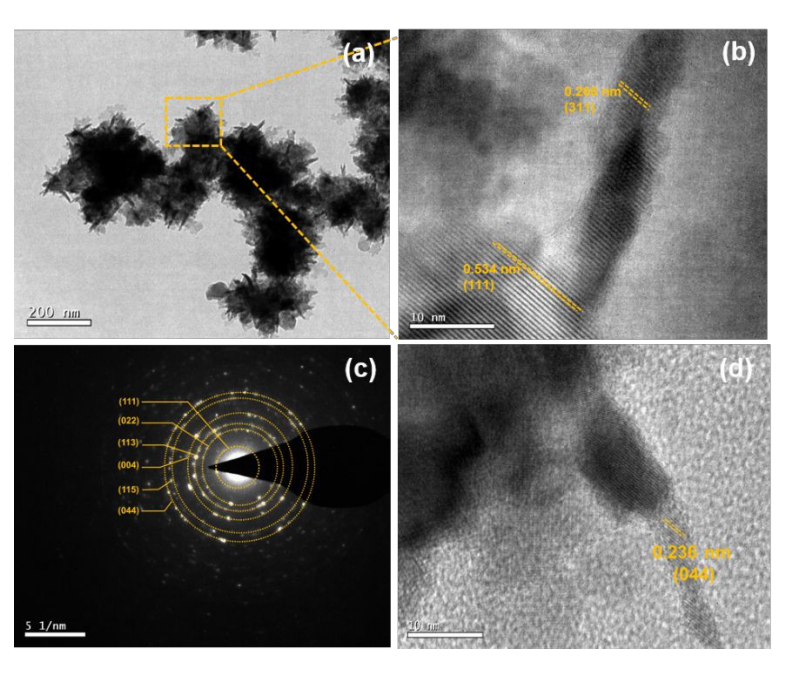


Figure 4: (a) low magnification TEM image of Fe_{0.03}CCS (b) HRTEM image of Fe_{0.03}CCS (c) SAED pattern of Fe_{0.03}CCS (d) HRTEM image of CCS.

Furthermore, transmission electron microscopy was employed to study the detailed interior structure of the catalyst. Figure 4(a) represent the bright field TEM image of Fe_{0.03}CCS at 200 nm displays 2D nanosheets morphology. In HRTEM analysis we found that the flat surfaces are predominantly exposed to (111) plane. In some cases, the perpendicular surface are exposed of (311) and (004) plane (Figure 4(b)). Figure 4(c) shows the selected area electron diffraction (SAED) with ring pattern indicating the polycrystalline nature of the catalyst. The SAED pattern

contains the diffraction from (111), (022), (113), (004), (115), and (044) planes of CCS which are consistent with the XRD result. Further Figure 4(d) represents the HRTEM image of CCS where perpendicular sheet with reflection from (004) plane.

The XPS survey spectrum shows the signal of Cu, Co, S and C for CCS, while for Fe-doped samples, the signal corresponding to Fe is also present without any additional peaks, demonstrating the purity of the synthesized catalyst (Figure 5(a) and (b)). The deconvolution of Co 2p spectra displayed two doublets corresponding to Co2p_{3/2} and Co2p_{1/2}. The deconvoluted spectra shows the peaks at 778.64 eV and 793.7 eV, characteristic peaks of Co³⁺, while the peaks at 780.5 and 796.1 eV correspond to Co²⁺ (Figure 5(c)). Two satellite peaks are also present in the deconvoluted data corresponding to Co2p_{3/2} and Co2p_{1/2}. Upon Fe-doping, the XPS spectra for the doped samples show almost negligible change in the Co 2p spectrum (Figure S3 (a)). Similarly, the Cu 2p spectra were deconvoluted into two doublets due to spin–orbit coupling. The peaks at 932.3 and 952.1 eV are attributed to Cu¹⁺, while the peaks at 934.2 and 955.5 are attributed to Cu²⁺ Figure 5(d). The

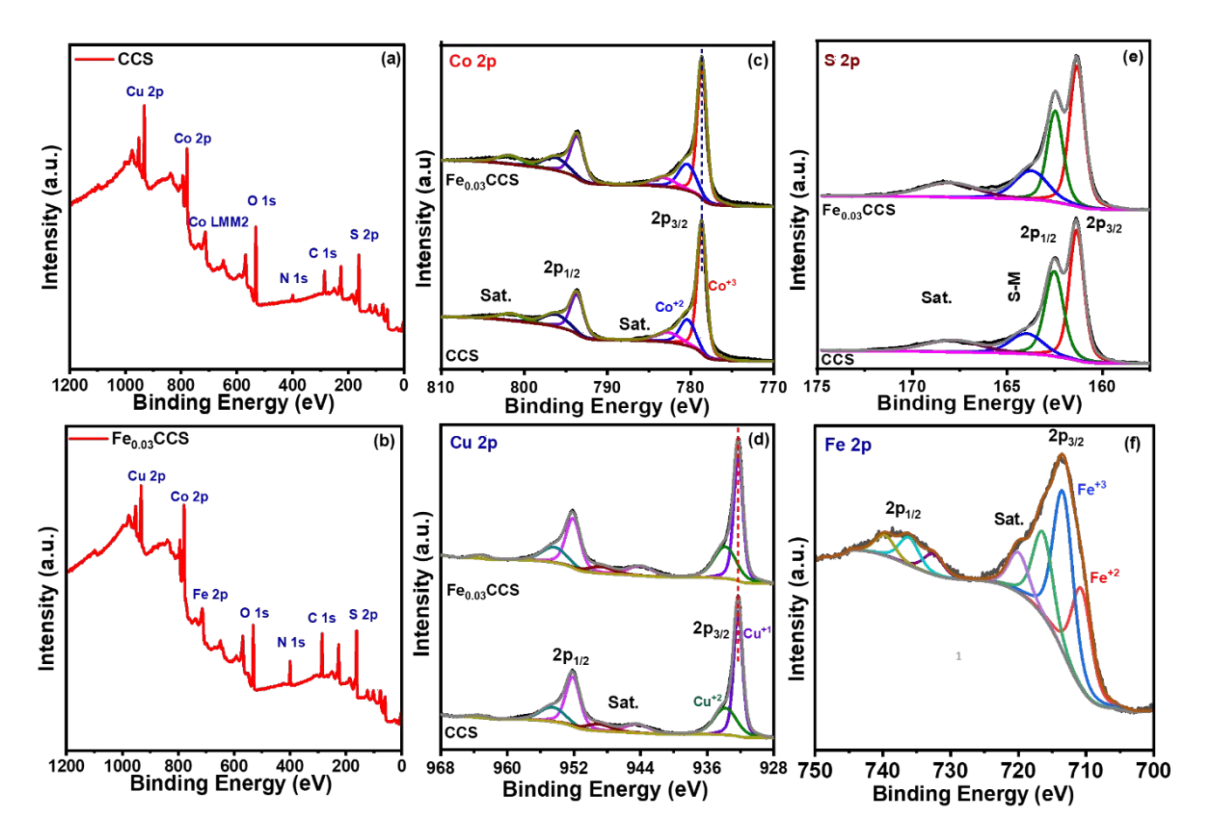


Figure 5: XPS survey spectrum of (a) CCS (b)Fe_{0.03}CCS, Deconvoluted XPS of CCS and Fe_{0.03}CCS (c) Co 2p (d) Cu 2p (e) S 2p (f) Deconvoluted XP spectra of Fe 2p for Fe_{0.03}CCS catalyst.

addition of Fe in the CCS structure shows no change in the XPS spectra (Figure S3 (b)). The S 2p

peaks were deconvoluted into a satellite peak (168.7 eV) and three peaks. The peaks at 161.6 and 162.7 eV are ascribed to S2p_{3/2} and S2p_{1/2}, respectively. The peak at 164.1 eV suggested the presence of sulfur metal (S–M) bond Figure 5(e). The deconvoluted Fe spectra show two spin-orbit doublets corresponding to 2p_{3/2} and 2p_{1/2}. The peaks at 710.7 and 732.8 eV correspond to Fe²⁺, while peaks at 713.4 and 736.1 eV represent Fe³⁺ Figure 5(f) and (Figure S3 (d)). The XPS depth profiling was also performed to investigate the elemental distribution from the surface to the bulk phase for Co2p, Cu 2p, Fe 2p and S 2p by sequential etching for 60s and 120s as shown in Figure S4 to Figure S7. After etching, the S 2p peak exhibited a slight shift toward higher binding energy, accompanied by the diminution of the satellite peak. This behavior suggests the removal of surface-adsorbed or reduced sulfur species and the exposure of more stoichiometric lattice sulfur. Meanwhile, the Fe 2p, Co 2p, and Cu 2p spectra showed no significant change in binding energy, although their intensities increased after etching, indicating that the oxidation states of the metal cations remain stable and that Fe is homogeneously distributed throughout the structure without surface segregation.

The electrochemical ORR activity of all samples was first examined by CV in N₂, followed by in O₂ saturated 0.1 M KOH electrolyte over a wide potential range from 0 to 1.014 V vs. RHE at a scan rate of 20 mV s⁻¹. As shown in Figure S8 (a) a featureless CV was observed in N₂ environment; however, subsequent studies in O₂ saturated 0.1 M KOH demonstrate a steep increase in reductive current density ascribed to ORR activity. Further, to gain insight into the ORR mechanism and kinetics, detailed experiments were performed under hydrodynamic conditions viz., RDE and RRDE measurements.

The RDE linear polarisation curves of various catalysts at a rotation rate of 1600 rpm at 5 mV s⁻¹ shown in Figure 6 (a) demonstrate a good onset potential and high diffusion-limited current density for all the catalysts. Remarkably, the optimized Fe_{0.03}CCS shows a comparable onset (0.89 V) and half-wave potential (0.80 V) respectively, and a higher diffusion-limited current density (Figure 6(a)). Figure 6(b) represents the bar graph comparison for at onset and half wave potential of all the catalyst. The Fe_{0.03}CCS catalyst performs better than other catalyst but still poorer than the commercial Pt/C. To further gain deeper insight of the ORR the RRDE measurements were conducted at different scan rate from 225 to 1600 rpm at 5mV s⁻¹ scan rate (Figure 6(c) and Figure S8(c) to (1)). With the increase in the rotation rate the reduction current density increases indicates

the faster diffusion of oxygen on the surface of catalyst with the increase in the mass transport current. To determine the mechanistic pathway for the ORR, further Koutecky–Levich (K–L) plots derived from RDE measurements at different potentials (Figure 6(c) and Figure S8), show good linearity between the reverse square root of rotation and reverse current density, confirming one step ORR process with first-order kinetics. The Figure 6(d) shows the ORR durability test. The ORR durability test were studied by running the CV in potential range from 1.01 to 0.61 V vs RHE at 100 mV s⁻¹ scan rate for 1000 cycles followed by LSV at 5 mV s⁻¹. The LSV before and after the durability test only shows 17 mV shift in the half wave potential with slight decrease in the current density.

Moreover, the Fe_{0.03}CCS shows excellent methanol tolerance and exhibit greater stability Figure 6(e). Figure 6(f) shows the no of electron transfer and H_2O_2 production for CCS and Fe_{0.03}CCS was calculated at different potential from 0.3 V to 0.7V vs RHE form the LSV curves of RRDE. The no of electron transferred for ORR process is close to 4 while H_2O_2 production yield is less than 5%. The number of electrons transferred was calculated from the RRDE plot and was found to be ca. 3.98 for Fe_{0.03}CCS with an average H_2O_2 production of 0.5–10%.

To probe the bifunctional activity, the OER activity of all the catalyst was evaluated by performing LSV at 5 mV s⁻¹ in the potential range of 1.22 V to 1.82 V vs. RHE. The OER activity was performed in 1 M KOH solution in N₂ saturated environment firstly, all the catalysts were examined by cyclic voltammetry in a wide potential range from 0.02 V to 1.62 V at a scan rate of 50 mV s⁻¹ (Figure S9 (a)). The Figure 6(g) shows the OER polarization curve for all the catalysts at a scan rate of 5 mV s⁻¹. The Fe_{0.03}CCS has a better onset potential as compared to CCS and other Fe-doped catalysts for OER. The Figure 6(h) shows the bar graph comparison for OER at different current density for all the synthesized catalysts with RuO₂. The Fe_{0.03}CCS catalyst having lowest overpotential (330 mV) at 10 mA cm⁻² current density.

Moreover, the current density of Fe_{0.03}CCS is far greater than that of CCS. The Fe_{0.03}CCS has a lower overpotential at 10 mA cm⁻² as compared to other synthesized catalysts. The Tafel plot was also determined from corresponding polarization curves (Figure 6(i)). The Fe_{0.03}CCS has a lower tafel slope (69.9 mV dec⁻¹) and faster kinetics for OER as compared to CCS (79.8 mV dec⁻¹). Figure 6(j) shows the Nyquist plot for the prepared catalyst. All the catalysts have similar solution resistance (Rs) as electrochemical studies were performed in the same electrolyte concentration.

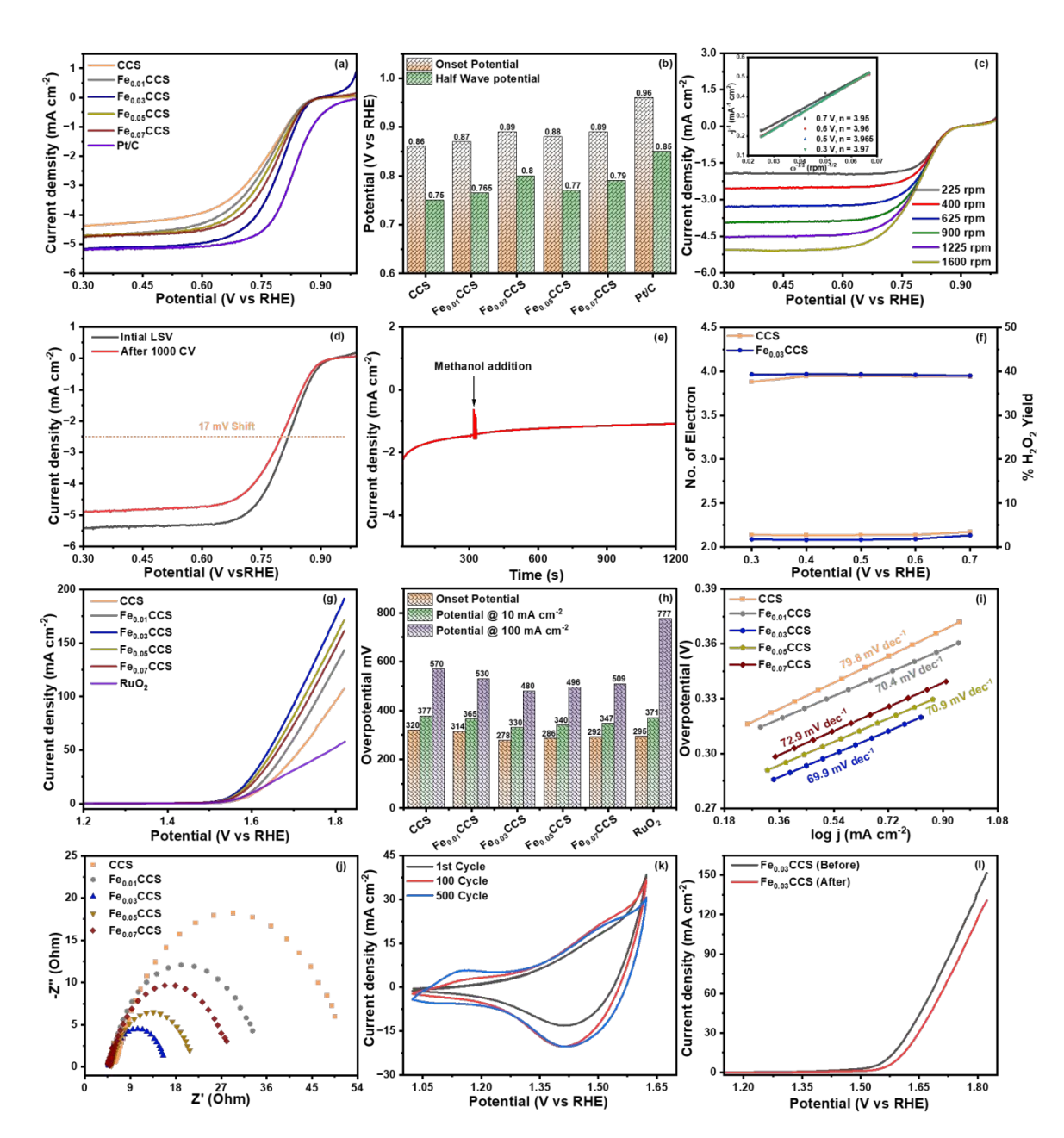


Figure 6: (a) ORR comparison plots of all the synthesized catalysts and 20% Pt/C in oxygen-saturated 0.1 M KOH at 1600 rpm in the potential window of 0.3 to 1 V vs. RHE at a scan rate of 5 mV s⁻¹ (b) Bar graph comparison of all the synthesized catalysts and 20% Pt/C (c) LSV plot of Fe_{0.03}CCS at different rotation rate from 225 to 1600 rpm at 5 mV s⁻¹ scan rate with inset showing Koutecky–Levich plot for Fe_{0.03}CCS catalysts at various potentials and the number of electrons transferred (d) ORR polarization comparison of Fe_{0.03}CCS after cycling in oxygen-saturated 0.1 M KOH for 1000 cycles (e) Methanol tolerance test for Fe_{0.03}CCS catalyst (f) No of electron tarnsfer and H₂O₂ percentage yield for CCS and Fe_{0.03}CCS at different potential based on RRDE data (g) OER comparison plot of all the synthesized catalysts and RuO₂ in 1 M KOH at 1600 rpm in the potential window of 1.2 to 1.82 V vs. RHE (h) Bar graph comparison of all the synthesized catalysts for OER at different current densities (i) Tafel plot with the corresponding Tafel slope values for all the synthesized catalyst (j) Nyquist plot (k) Acceleration durability test showing 1st, 100 and 500 cycles (l) LSV polarization comparison of Fe_{0.03}CCS after cycling in nitrogen saturated 1 M KOH for 500 cycles

The Fe_{0.03}CCS shows a lower value of charge transfer resistance as compared to the pristine CCS catalyst. The acceleration durability test (ADT) was also conducted to study the long-term durability of the Fe_{0.03}CCS catalyst. The ADT was performed from 1.04V vs 1.65V vs RHE at 100mV/s (Figure 6 (k)) and Figure S9 (b). Initial cycles show quite good stability with an increase in the oxidation state, even after the 500 cycles the OER performance shown greater stability (Figure 6 (l)).

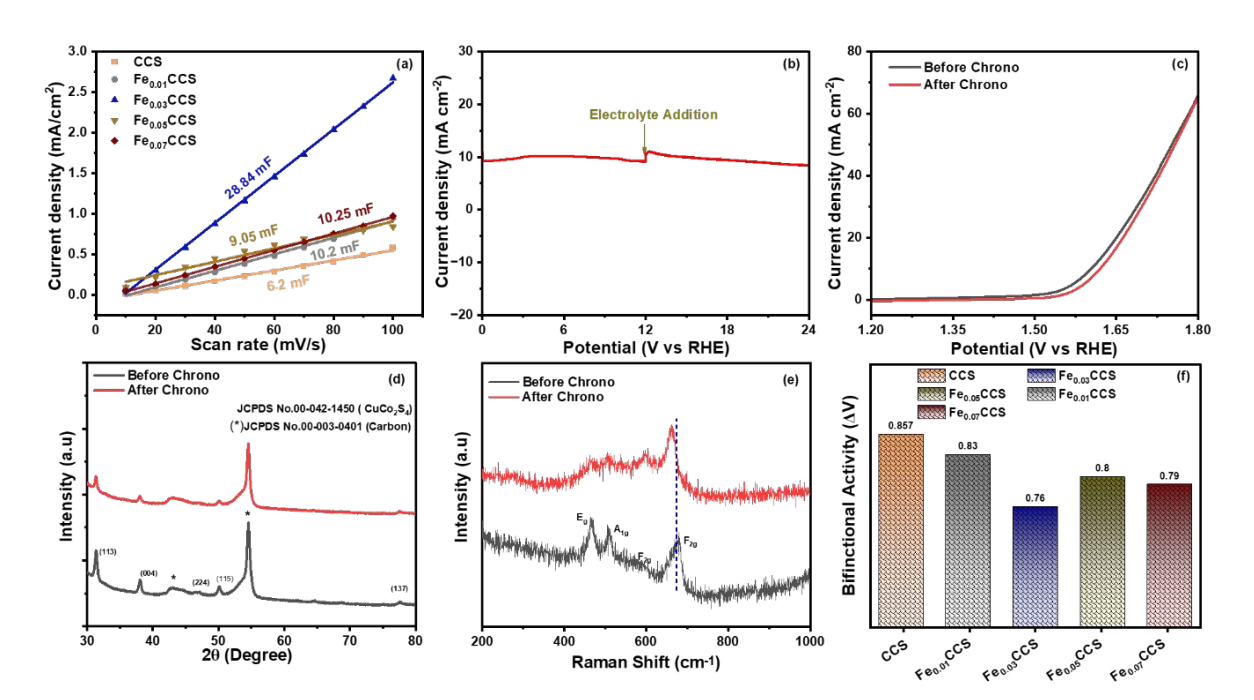


Figure 7: (a) Electrochemical active surface area (ECSA) of all the synthesized catalysts under EDLC region (b) Chronoamperometric response of Fe_{0.03}CCS in oxygen-saturated 1 M KOH (c) LSV polarization comparison of Fe_{0.03}CCS before and after chronoamperpometry study (d) XRD before and after 24h chrono study (e) Raman spectra before and after 24h chrono study (f) Bifunctional activity bar graph.

The electrochemical double layer (Cdl) was estimated by cyclic voltammetry from potential window 1.12V – 1.22V vs RHE at different scan rate from 10 to 100 mV/s (Figure S9 (c) to (l)). Double layer capacitance was determined from the slope of current density vs scan rate. The Figure 7 (a) shows the Cdl value for all the prepared catalyst where Fe0.03 having the highest value of Cdl 28.84 mF as compared to pristine CCS 6.02 mF. The long-term stability was studied with chronoamperometry at 10 mA/cm² current density on the carbon paper (Figure 7(b)). The Figure 7(b) shows a chronoamperometry study at 10 mA cm⁻² for 24 h, which exhibits a stable nature of

the catalyst with minimal reduction in the current density. The post-catalysis analysis was also performed before and after the chrono study. The XRD and Raman spectra show no change in the peaks before and after the chronoamperometric test, indicating good recyclability of the catalyst (Figure 7(d) and (e)). The excellent oxygen electrocatalytic activity of Fe_{0.03}CCS catalyst make the potential candidate for metal air battery as an air electrode. The difference in potential ΔE (where $\Delta E = E_{j=10 \text{ mA cm}^{-2}(\text{OER})} - E_{1/2 \text{ (ORR})}$) where $E_{j=10}$ is the potential required to produce 10 mA cm⁻² current density for OER and $E_{1/2}$ is the half-wave potential for the ORR) was the measure of the bifunctional activity for the oxygen electrocatalyst. The smaller value of ΔE indicates the improved bi-functionality of Fe-doped spinel. Figure 7(f) shows the bifunctional activity bar graph for all the catalysts and Fe_{0.03}CCS catalyst shows the lowest ΔE value of 0.76 V, indicating its superiority over the other catalysts. Table S5 represents the $E_{1/2 \text{ (ORR)}}$, $E_{j=10 \text{ mA cm}^{-2}(\text{OER})}$ and ΔE value of various other catalyst reported, where our catalyst exhibit greater performance as compared to other catalyst.

All State Zn-air battery Testing

In order to assess Fe_{0.03}CCS's possible use in storage devices, we built a standard Zn–air battery and measured it's battery performance in alkaline medium. An aqueous battery was assembled using a Fe_{0.03}CCS air cathode and a Zn foil anode in 6 M KOH + 0.2 M zinc acetate electrolyte. For comparison, a pristine CCS catalyst-based zinc air battery was also made. The open circuit potential for the Fe_{0.03}CCS-based battery is approximately 1.43 V, as shown in Figure 8(a) and it stays constant even after 24 hours while the pristine CCS battery shows OCP value of 1.35V. The battery's energy storage capacity, measured at 5 mA cm⁻², showed a voltage platform at 1.20 V, resulting in a specific capacity of 803.4 mA h g⁻¹ normalized with the mass of lost zinc and CCS based battery has a value of 748.8 mA h g⁻¹ (Figure 8(b)). Figure 8(b) inset shows the bar graph of discharge test for Fe_{0.03}CCS aqueous zinc air battery at different current densities ranging from 2 to 20 mA cm⁻². The specific capacity of aqueous zinc air battery is calculated by discharging at a specific current density and regularized by the weight of zinc consumed in the process. The specific capacity at 2 mA cm⁻², 5 mA cm⁻², 10 mA cm⁻² and 20 mA cm⁻² was 804.1 mA h g⁻¹, 801.9 mA h g⁻¹, 799. 8 mA h g⁻¹ and 793.6 mA h g⁻¹ Figure S10 (a). Figure 8(c) shows the step discharge for both the catalysts CCS and Fe_{0.03}CCS at various current density ranging from 1 to 20 mA cm⁻². The discharge potential for CCS decreases more as compared to Fe_{0.03}CCS when current density

reached to 20 mA cm⁻². The peak power density of the Fe_{0.03}CCS catalyst is 82 mW cm⁻², and peak power density of CCS is only 52 mW cm⁻² as illustrated in Figure 8(d). Furthermore, the efficiency and long-term durability were then investigated by galvanostatic charge—discharge at a constant current density of 5 mA cm⁻² for 10 minutes of charging and discharging at –5 mA cm⁻² for 10 minutes (Figure 9(a)).

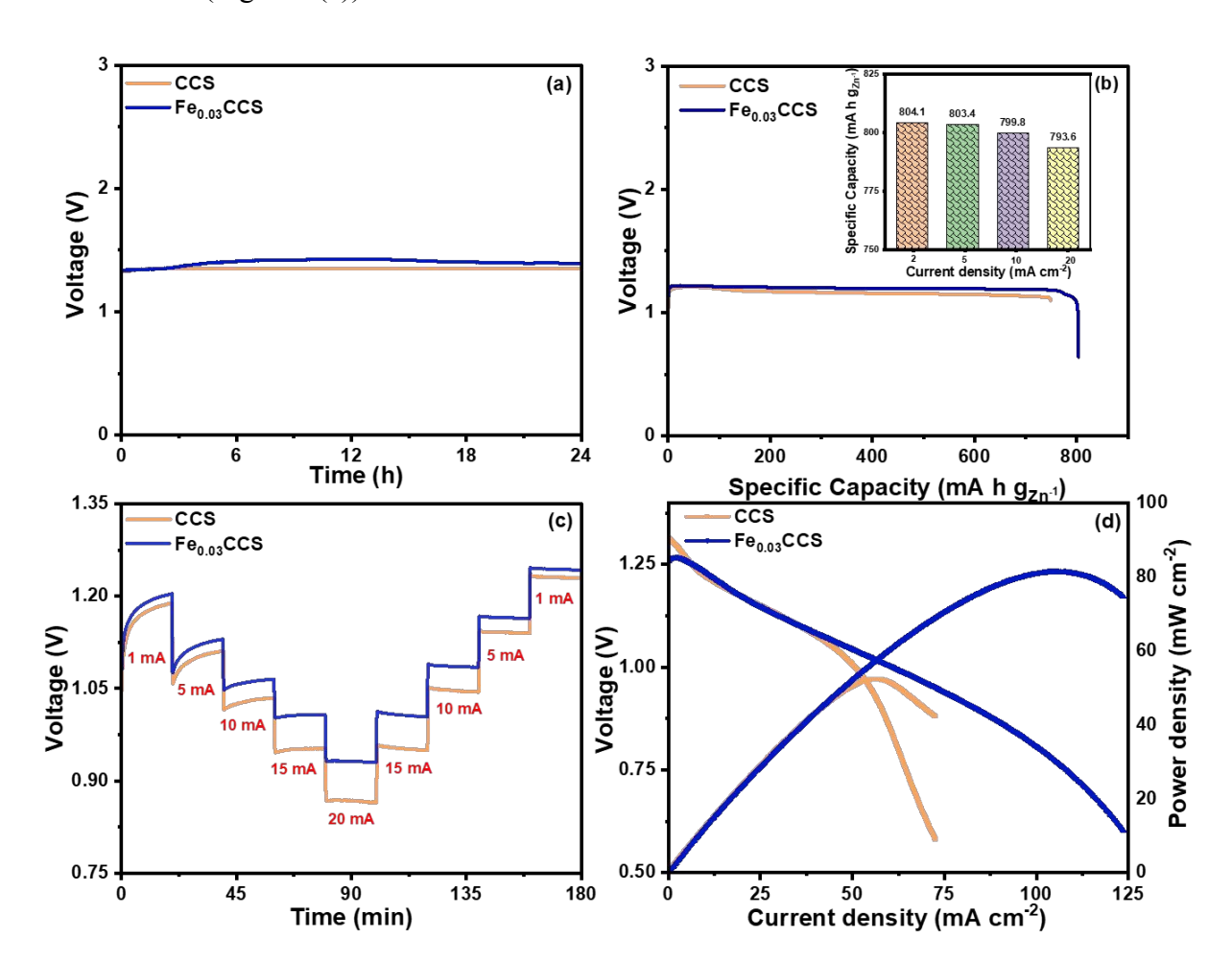


Figure 8: Aqueous Zn–air battery performance using CCS and Fe_{0.03}CCS as an air cathodes (a) open circuit potential (b) Specific capacity at 5 mA cm⁻² current density (inset showing bar graph of aqueous zinc air battery at different current densities ranging from 2 to 20 mA cm⁻² (c) the step discharge at various current density ranging from 1 to 20 mA cm⁻² (d) discharge polarisation curves and the corresponding power densities.

More importantly, negligible fading in the performance was observed even after 75 h and 210 cycles. During the intial period of battery performance the voltage gap is low with high round trip efficiency of 61.7% (Figure 9(b)). Even after the 100 cycles of GCD the voltage gap increased to

0.88V with a round trip efficiency of 56.65% (Figure 9(c)). For comparison, the Galvanostatic charge discharge performance of CCS is also conducted under similar conditions. In contrast in the CCS based battery the voltage gap increases drastically after the 60 hours show poor oxygen bifunctional activity.

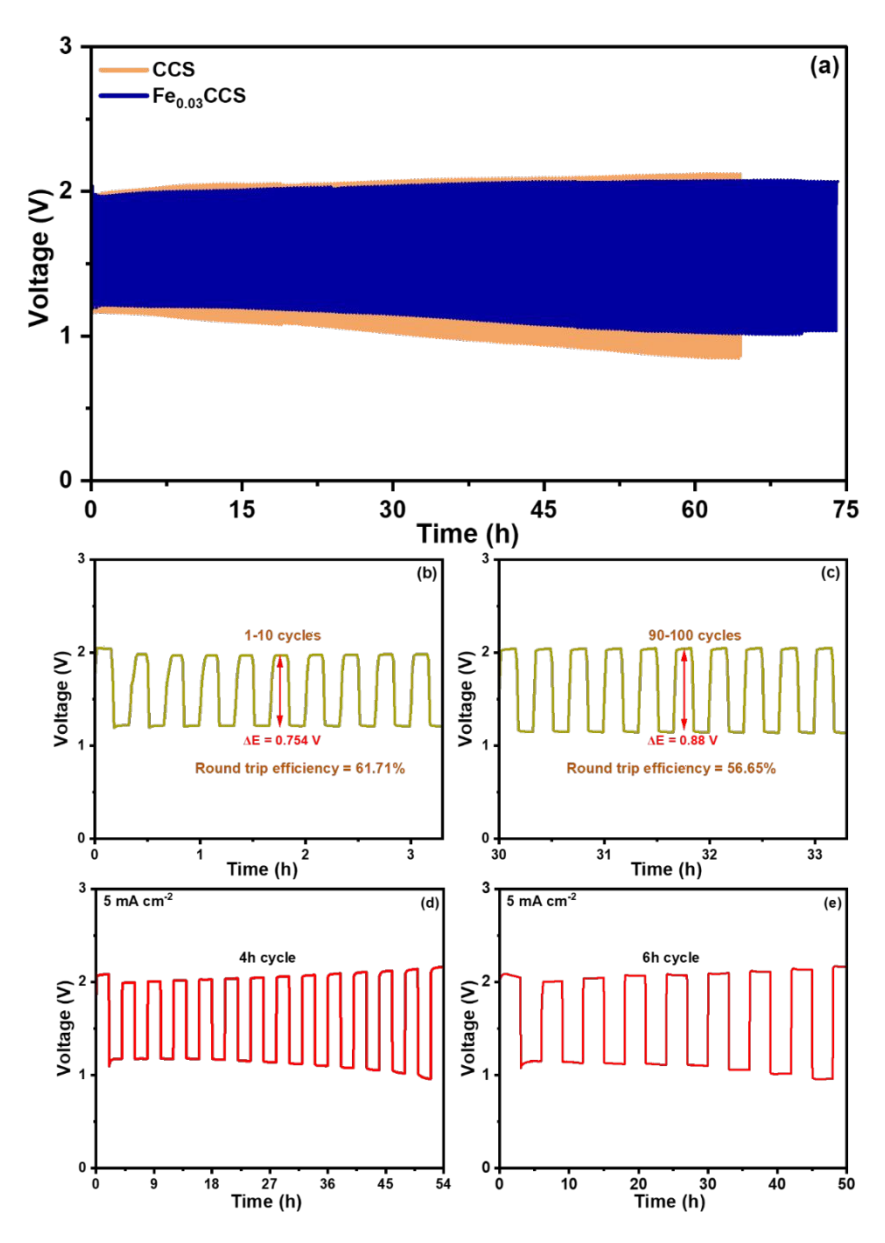


Figure 9: Galvanostatic charge discharge curve at 5mA cm⁻² for 10 minute charge discharge cycle. (b) and (c) Corresponding round trip efficiency calculation at 1-10 cycles and 90-100 cycles respectively. Galvanostatic charge–discharge plot of Fe_{0.03}CCS zinc–air battery at a current density of 5 mA cm⁻² with (d) 4 h per cycle (e) 6 h per cycle.

Most of the research article reported on zinc air battery only shows the Galvanostatic charge discharge for 20 minutes per cycle. To evaluate the performance for practical applications it is necessary to conduct longer charge discharge. As during longer discharge time the zincate ion gets saturated and forms the insoluble zinc oxide in the electrolyte which restricts the performance of zinc air battery. While during the longer charging time the dendrites growth increases which increases the voltage during charging.

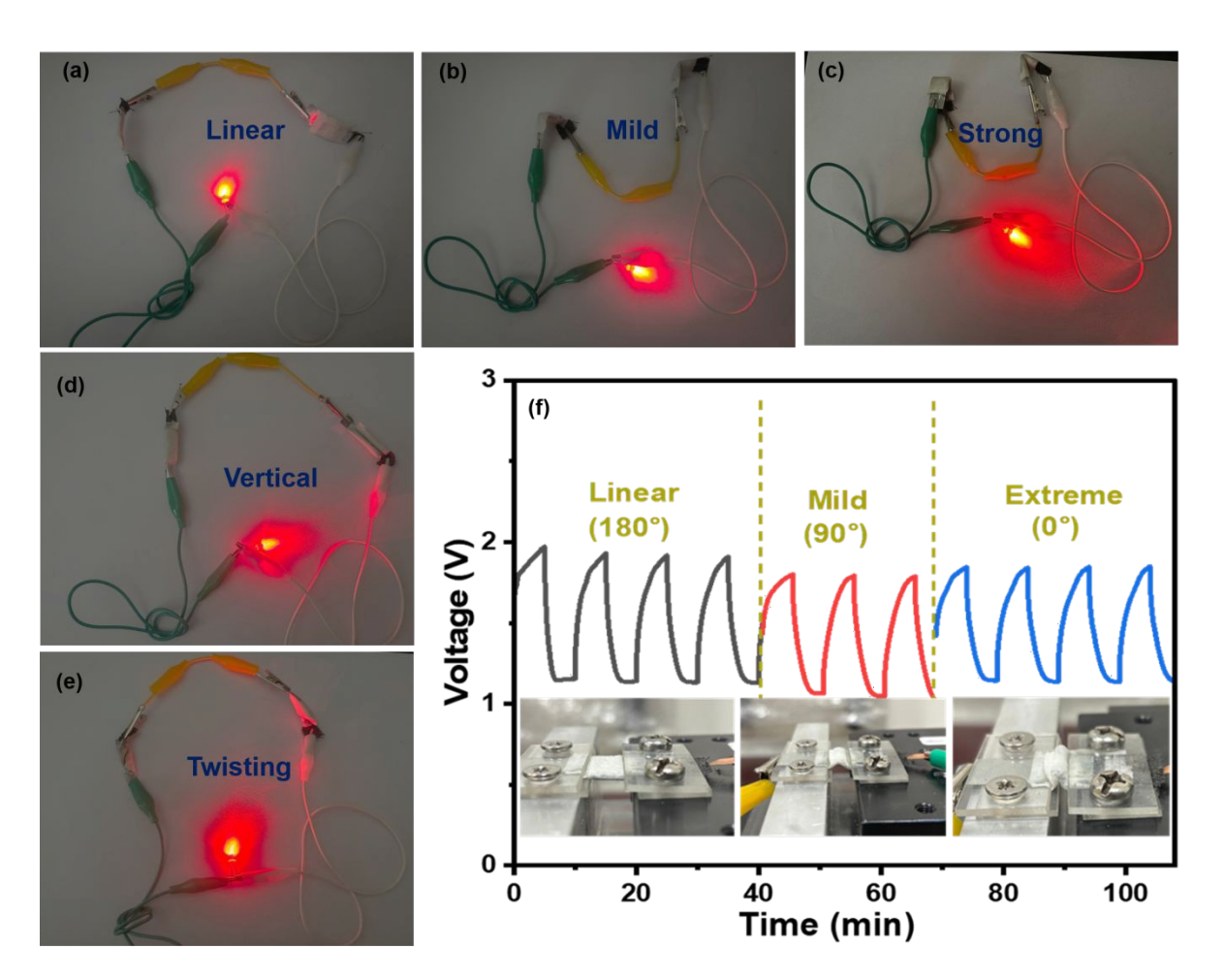


Figure 10. (a) to (e) Digital photographs of the foldable ZABs at different bending angles to light an LED lamp (f) Discharge–charge curves of Fe_{0.03}CCS in foldable ZABs at various bending angles.

To study the effect of longer charge discharge, we have conducted the Galvanostatic charge discharge at 4h per cycle and 6h per cycle. In the 4h per cycle the battery could easily ran for 54 hour with small increase in the voltage gap with lesser amount of zinc oxide formation and small increased polarization (Figure 9(d)). While for 6 h per cycle the initial 8 cycles show smaller voltage gap and battery run for 50 hours (Figure 9(e)). After this both the charging and discharging

Furthermore, a solid-state zinc air battery of Fe_{0.03}CCS catalyst was assembled using a solid-state polymer as an electrolyte. Figure 10 shows Digital photographs of the foldable ZABs at different bending angles to light an LED lamp. Discharge-charge curves of Fe_{0.03}CCS in foldable ZABs at various bending angles. The measurement data show that the battery was efficient for all the bending angles.

The assembled solid-state zinc air battery shows an OCP value of 1.37 V, which is slightly less than the aqueous battery due to the internal resistance of the solid-state electrolyte (Figure 11(a)). Even when the two solid state batteries were connected in series the OCP value almost doubled 2.706V (Figure 11(b)). By using two solid state batteries we could glow an LED, showing a reallife demonstration of our catalyst (Figure 11 (c)). Figure 11(d) shows the Galvanostatic charge discharge plot of the Fe_{0.03}CCS catalyst at 2 mA cm⁻² with 5 min of charge and 5 min of discharge

This article is licensed under a Creative Commons Attribution-NonCommercial 3.0 Unported Licence

Open Access Article. Published on 18 Tachwedd 2025. Downloaded on 19/11/2025 05:45:50.

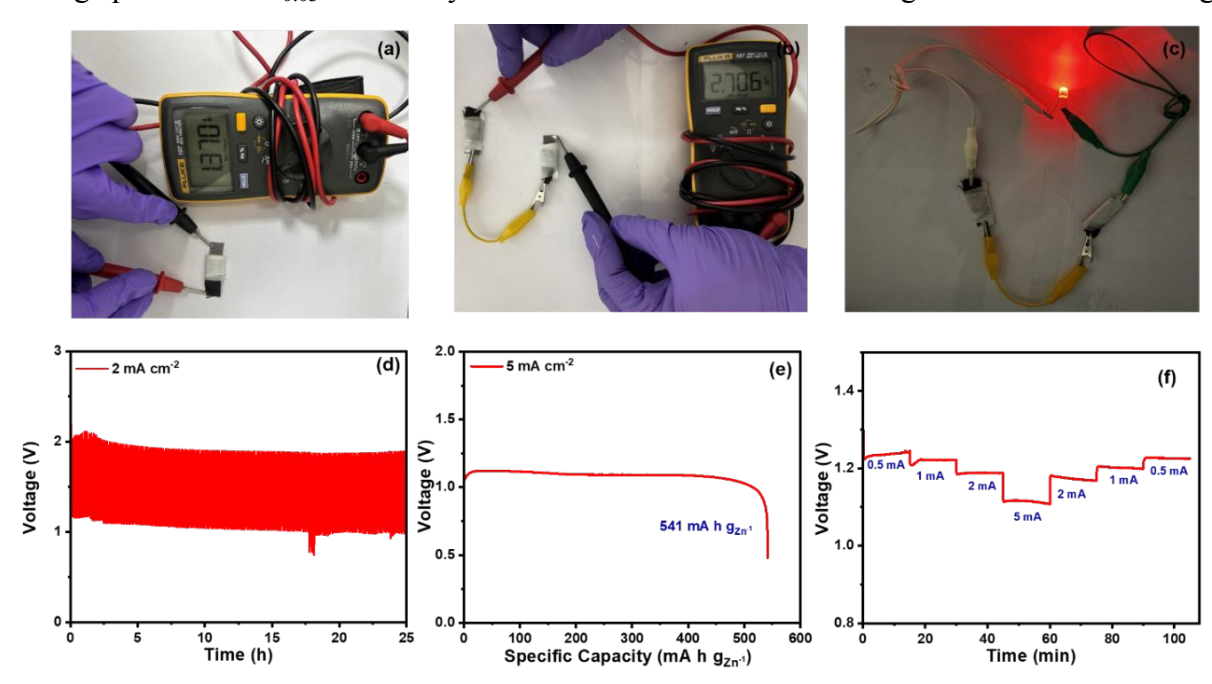


Figure 11: (a) Assembly of solid-state zinc-air battery of Fe_{0.03}CCS with OCP showing 1.37V (b)Two solid-state zinc-air battery of Fe_{0.03}CCS connected in series with OCP showing 2.706V (c) Image of Fe_{0.03}CCS based zinc–air battery-powered LED (d) Galvanostatic charge discharge of solid state zinc air battery at 2 mA cm⁻² current density (e) Plot showing discharge capacity of Fe_{0.03}CCS based solidstate zinc air battery at 5 mA cm⁻² (f) Step discharge of Fe_{0.03}CCS at different discharge current density

cycle. The GCD shows stability of 25h with a small change in the voltage gap, showing good durability of our catalyst in the solid-state condition.

Additionally, Figure 11(e) shows the specific capacity of the Fe_{0.03}CCS catalyst at 5 mA cm⁻². The zinc foil was mechanically scratched, and the amount lost was used to calculate the specific capacity of solid state battery. Additionally, we have performed the discharge testing of Fe_{0.03}CCS solid state zinc air battery at various current density from 1 to 10 mA cm⁻² Figure S10(b). Figure 11(f) shows the step discharge of solid state battery at different current densities ranging from 0.5 mA to 5 mA cm⁻². The step discharge of Fe_{0.03}CCS catalyst shows good stability at all current densities and has better reversibility. The Fe_{0.03}CCS catalyst shows promising behavior for real-life zinc air battery application. These results illustrate that Fe_{0.03}CCS is a promising alternative to noble metal-based catalysts and can be successfully used as an air cathode for Zn–air batteries.

Theoretical Analysis

In order to have a deeper understanding of the underlying mechanism of electrocatalytic OER-ORR performance on $CuCo_2S_4$ (113) surface, we have performed first principle calculations under the framework of Density Functional Theory (DFT). To model the experimentally synthesized structure we have cleaved (113) plane for both pristine $CuCo_2S_4$ (CCS) and Fe doped $CuCo_2S_4$ [Fe_xCuCo₂S₄] surface from the bulk.

Our theoretical investigation of OER-ORR activity is mainly based on the Nørskov's approach³¹ of reaction coordinate mapping. According to this approach, for a good OER-ORR catalyst, all the reaction steps involved in the process should have a free energy change (ΔG) close to 1.23 eV as the redox potential for water splitting is 1.23 V. This ensures that the catalyst should bind with reaction intermediates (O*, OH*, OOH*) neither too strongly nor too weakly, for the reaction to happen without applying significant amount of external bias. The free energy of the adsorbed intermediates on the catalyst surface can be determined using the following equation: $\Delta G_X^* = E_{ads}^X + \Delta ZPE - T\Delta S$, where X are the intermediates O*, OH* and OOH*. E_{ads}^X gives the adsorption energy of the intermediates and ($\Delta ZPE - T\Delta S$) is the correction due to zero-point energy and entropic contribution between the adsorbed state and the free state of each intermediates.

The oxygen evolution reaction (OER) in aqueous solutions proceeds via the direct four-electron oxidation of water (H₂O) to oxygen (O₂) which leads to oxygen evolution.

$$2H_2O \rightarrow O_2 + 4H^+ + 4e^- (E^0 = +1.23 \text{ V vs SHE})$$

The free energy change for the four elementary steps of OER can be obtained as $\Delta G_1 = \Delta G_{OH}^*$ - $\Delta G_{H_2O_2} \Delta G_2 = \Delta G_O^* - \Delta G_{OH}^*, \Delta G_3 = \Delta G_{OOH}^* - \Delta G_O^*, \Delta G_4 = \Delta G_{O_2} - \Delta G_{OOH}^*.$ The maximum free energy change $\Delta G_{\text{max}} = \text{max} \left[\Delta G_1, \Delta G_2, \Delta G_3, \Delta G_4 \right]$ among these four steps defines the potential needed to make OER thermodynamically favourable, i.e. all steps must be downhill. That extra potential is known as overpotential, defined as how much extra potential (voltage) that must be applied beyond the thermodynamic equilibrium potential to drive the reaction. For OER, the overpotential (η_{OER}) is given by the formula

$$\eta \text{OER} = \frac{\Delta Gmax}{e} - 1.23$$

Free energy values on pristine and doped surfaces for Oxygen Evolution Reaction (OER) are summarized in Table 1.

Table 1: Gibbs free energy values for all active sites in pristine and doped CuCo₂S₄ in OER pathway

Surface(OER)	Active site *	ΔG_1 (eV)	ΔG_2 (eV)	ΔG_3 (eV)	ΔG_4 (eV)	$oldsymbol{\eta_{ ext{OER}}}{ ext{(V)}}$
CuCo ₂ S ₄ (CCS)	Co	-0.08	0.95	2.19	1.84	0.96
(CCS)	Cu	1.32	-0.51	3.19	0.93	1.96
CuCoFeS ₄	Со	0.42	1.42	1.72	1.36	0.49
$(Fe_xCuCo_2S_{4)}$	Cu	1.19	0.19	2.98	0.56	1.75
	Fe	-o.11	0.53	2.10	2.39	1.17

From the Table 1, it is observed that, when we consider pristine CCS surface, Co site has the lower overpotential of 0.97 V as compared to 1.96 V on top of Cu which indicates relatively poor OER performance on Cu site. If Co acts as the active site we need to apply at least 2.19 V bias to make all OER steps thermodynamically favorable i.e. exothermic, which gives rise to an overpotential of 0.96 V. Figure 12(a) and (b) shows the corresponding free energy profile for OER on pristing CuCo_2S_4 surface. Both from the table as well as from the free energy profile it can be inferred that, the formation of OOH* is the potential determining step with largest positive ΔG_n value on both the active sites.

On the other hand, when we consider the doped surface, the overpotential values are found to decrease significantly on some of the active sites, upon doping with Fe. For doped surface also, Co site turns out to be the best possible active site with lowest overpotential among all the considered active sites. Figure 12(c) shows the η_{OER} reduces from 0.96 V to 0.49 V on top of Co while small change is observed in case of Cu, reducing from 1.96 V to 1.75 V (Figure 11(d)). Fe site performs better than Cu but poorer than Co with an overpotential of 1.17 V (Figure 11(e)). It is anticipated that the substitutional doping alters the local electronic structure which have a direct impact on the electron transfer between the surface and adsorbate and hence helps to facilitate the OER process. This result matches well with the experimental outcome where the doped surface is found to exhibit enhanced OER catalytic performance.

The oxygen reduction reaction (ORR) in which molecular oxygen (O_2) is reduced to water (H_2O), follows exactly the reverse steps of OER while involving the same reaction intermediates *i.e.* OH*, O* and OOH*.

$$O_2 + 4H^+ + 4e^- \rightarrow 2H_2O (E^0 = +1.23 \text{ V vs SHE})$$

Similar to the case of OER, the free energy changes for the four elementary steps of ORR can be obtained as $\Delta G_1 = \Delta G_{OOH}^* - \Delta G_{O_2}$, $\Delta G_2 = \Delta G_O^* - \Delta G_{OOH}^*$, $\Delta G_3 = \Delta G_{OH}^* - \Delta G_O^*$, $\Delta G_4 = \Delta G_{H_2O} - \Delta G_{OH}^*$. The theoretical overpotential for ORR is calculated as follows:

$$\eta ORR = \frac{\Delta Gmax}{e} + 1.23 V$$

The adsorption free energies for ORR are summarized in the Table 2.

Table 2: Gibbs free energy values for all active sites in pristine and doped CuCo₂S₄ in ORR pathway

Surface(ORR)	Active site	Δ G ₁ (eV)	ΔG_2 (eV)	ΔG_3 (eV)	ΔG_4 (eV)	$oldsymbol{\eta_{ m ORR}}{ m (V)}$
	*					
CuCo ₂ S ₄	Co	-1.84	-2.19	-0.95	0.08	1.31

(CCS)	Cu	-0.93	-3.19	0.51	-1.32	1.74
CuCoFeS ₄	Co	-1.36	-1.72	-1.42	-0.42	0.81
(Fe _x CuCo ₂ S ₄₎	Cu	-0.56	-2.98	-0.19	-1.19	1.04
	Fe	-2.39	-2.1	-0.53	0.11	1.34

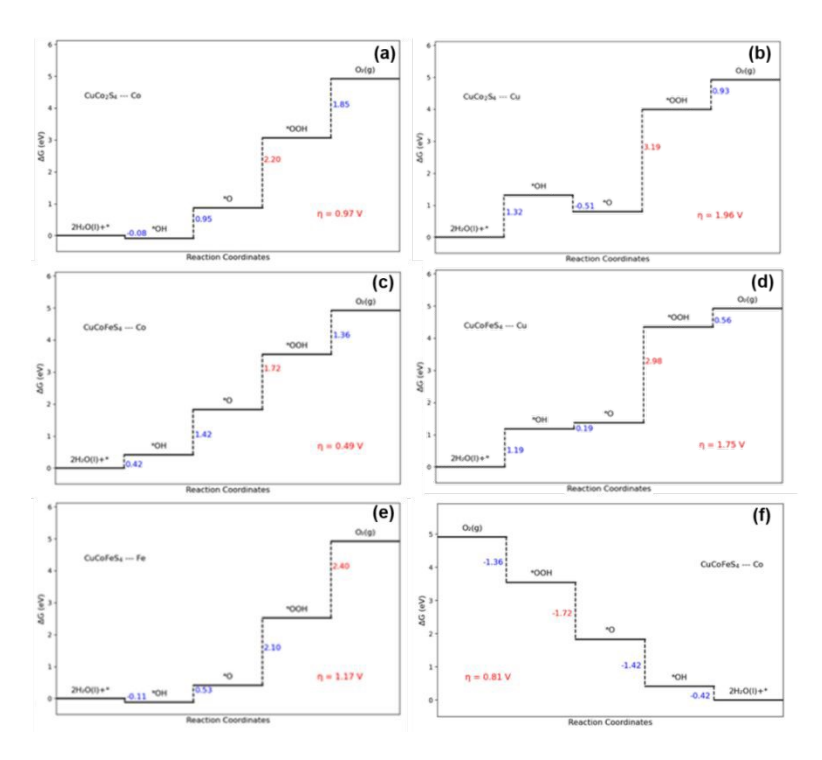


Figure 12: Free energy profile on (a) Co (b) Cu active sites in CuCo₂S₄ for OER mechanism Free energy profile in CuCoFeS₄ for OER mechanism on (c) Co (d) Cu and (e) Fe active sites (f) Free energy profile on Co active site in CuCoFeS₄ for ORR mechanism

Ideally in ORR all the steps are exothermic at zero applied bias. When we study ORR mechanism on pristine CCS surface, we observe that there exists no such adsorption site which could facilitate the process with all the four steps being exothermic at zero applied bias. It is evident from Table 2 that, on Co and Cu active sites, ΔG_4 and ΔG_3 steps are uphill respectively, indicating thermodynamically unfavourable ORR kinetics. Between Co and Cu, Co has the lower overpotential of 1.31 V.

On the other hand, when we consider ORR on Co and Cu sites of Fe_xCuCo₂S₄ surface, all the four steps are found to exhibit exothermic nature at zero applied bias. Figure 12(f) shows the free energy profile for ORR on Co active site of doped CuCo₂S₄ surface. Cu as an active site has the slightly higher overpotential of 1.04 V than that of Co with η_{ORR} value ~0.81 V. While Fe shows poor catalytic performance for ORR due to positive ΔG_4 which leads to high overpotential of 1.34 V. This result suggests that, Fe doping reduces the ORR overpotential on Co site from 1.31 V in pristine surface to 0.81 V in doped surface by making ΔG_4 step downhill. A Similar observation is found for Cu site, overpotential reducing from 1.74 V to 1.04 V but by making ΔG_3 downhill. We have calculated both adsorption energy as well as free energy changes for the three reaction intermediates namely OH*, O*, and OOH* (where * represents intermediate adsorbed on the catalyst surface), but in the table provided in the manuscript only free energy changes required to map the free energy profile diagram were given. We have also clearly mentioned both the adsorption energy as well as free energy changes for the intermediate adsorption on both pristine and doped catalyst surfaces in Table S6-7. The adsorption energy was calculated for the adsorption of H₂O and O₂ on all possible active sites of pristine and doped surface which completes the calculations for the whole range of intermediates. From the adsorption energy values, it is evident that both H₂O and O₂ are chemisorbed on the pristine CuCo₂S₄ surface. Upon doping the binding energies change significantly with ΔG values closer to thermoneutral condition. This suggests that, initial intermediates (i.e. H₂O in case of OER and O₂ in case of ORR) neither binds too strongly nor too weakly on the doped CuCoFeS₄ surface and thereby making it better catalyst for facilitating the OER and ORR processes. The optimized geometries of H₂O and O₂ adsorption on pristine and doped surfaces are depicted in Figure S14 – S17.

In addition, to the free energy profiles for overpotential calculations, we have also investigated the band structure and atom projected density of states (DOS), which shows metallic nature for both the pristine and doped surfaces. It is anticipated that metallic surface acts as the source of free electrons for accelerating the catalytic process. The band structure and density of states plots are depicted in Figure 13.

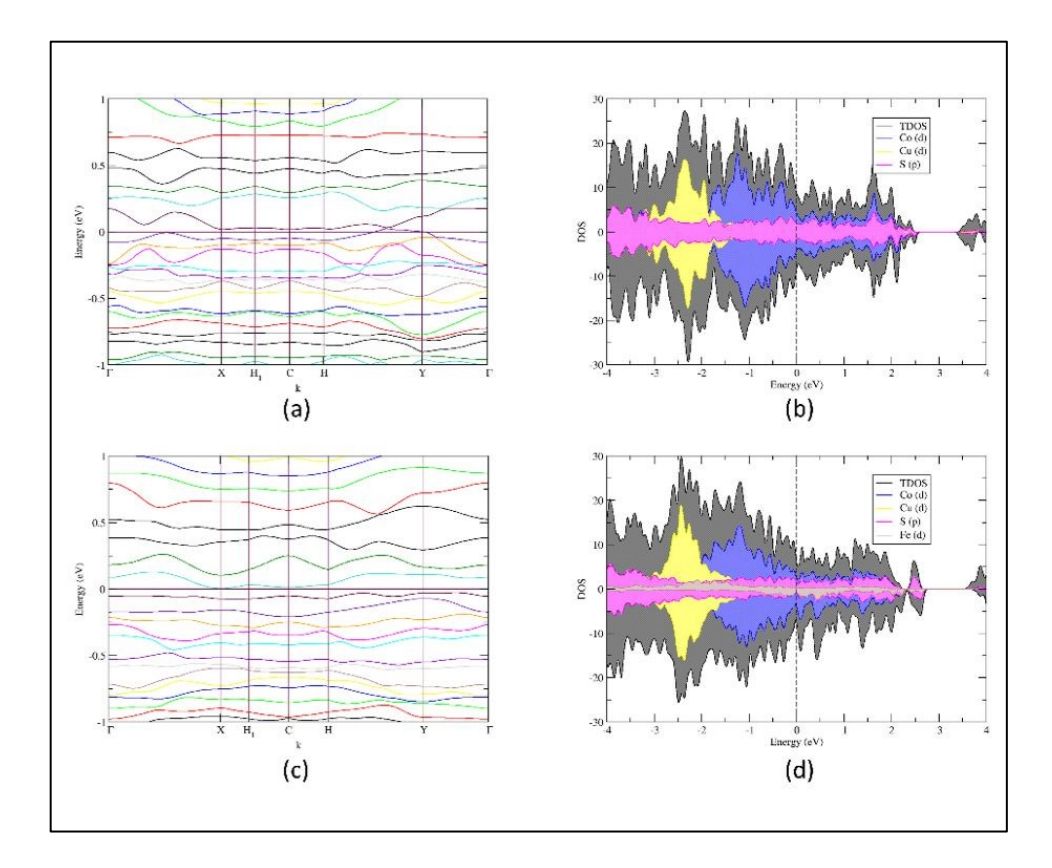


Figure 13: Bands structure and Density of states for (a) (b) pristing and (c) (d) doped surfaces respectively.

The atom projected density of states shows major contribution of Co-d orbitals near the Fermi level in the valence band of CuCo₂S₄, which acts as a potential source of electrons and thus plays a crucial role in the overall OER and ORR process. The doped surface also shows similar kind of behaviour. This is also reflected in the free energy profile, which shows among all the considered active sites. Co acts as the best possible site with lowest overpotential both for OER and ORR in the pristine as well as doped surfaces.

These results suggest that the Fe doping is found to be beneficial for enhancing both OER and ORR catalytic performance and thus can be used as an alternative cathode material for rechargeable Zn air battery. Detailed XRD analysis indicates the existence of an optimum dopant concentration, beyond which new phase formation begins. Rietveld refinement confirms trace amounts of Cu₂S in all samples, with pristine CuCo₂S₄ exhibiting the highest content. Upon Fe incorporation, the Cu₂S phase decreases, correlating with enhanced OER and ORR performance. Both electrochemical measurements reveal that Fe doping in CCS must be carefully optimized, as excess Fe (>125 ppb) induces the formation of catalytically inferior FeS. Converging evidence from XRD, Raman spectroscopy, and XPS suggests that excessive FeS formation adversely affects oxygen reduction due to the reduction of catalytically active sites in thio-spinel. Microstructural characterization, electrochemical studies, and DFT calculations consistently identify Fe_{0.03}CCS as the most effective catalyst. Detailed electrochemical analysis further confirms that new phase formation degrades catalytic activity. The pristine $CuCo_2S_4$ catalyst exhibits bifunctional performance, achieving a half-wave potential of 0.76 V vs RHE for the ORR and an OER overpotential of 370 mV at 10 mA cm⁻² ($\Delta E = 0.84$ V), resulting in a peak power density of 52 mW cm⁻² and a specific capacity of 748.8 mAh gZn⁻¹ in Zn-air batteries. Fe incorporation enhances these metrics, yielding a half-wave potential of 0.80 V and an OER overpotential of 330 mV ($\Delta E = 0.76$ V), corresponding to an impressive power density of 82 mW cm⁻² and a specific capacity of 803.4 mAh gZn⁻¹. DFT calculations corroborate these findings, revealing that the initial intermediates (H₂O for OER and O₂ for ORR) bind neither too strongly nor too weakly on the Fe-doped $CuCo_2S_4$ surface, thereby facilitating efficient bifunctional oxygen electrocatalysis.

Conclusion

In summary, we report a single-step hydrothermal approach for synthesizing Fe-doped CuCo₂S₄ thio-spinel. A series of Fe_xCuCo₂S₄ was successfully synthesized and demonstrated as an oxygen bifunctional electrocatalyst for both aqueous and solid rechargeable zinc air batteries. The extensive experimental and theoretical investigation strongly suggests that Fe doping has a significant effect on oxygen electrocatalysis. The impact of Fe doping on the Oh site effectively tune the e_g occupancy of Co and therefore improved oxygen electrocatalysis. The Fe doping in CuCo₂S₄ crystal increase the active site concentration (Cdl ~ 28.84 mF) as compared to pure CuCo₂S₄ having Cdl 6.2 mF. The Galvanostatic charge-discharge shows excellent stability for 75 hours with more than 200 cycles. Moreover, the solid state battery of Fe_{0.03}CCS shows good stability for 25 hours with a specific capacity of 541 mAhg_{Zn}-1. The demonstrated solid state battery can glow the LED shows a real-life application of our optimized catalyst. The demonstrated zinc air battery with Fe_{0.03}CCS as an air cathode shows excellent activity and higher stability. The Fe insertion into the thiospinel structure increases the catalytically active sites, which enhances the oxygen bifunctional behavior making it a potential catalyst for advanced zinc air battery applications. The outstanding durability and flexibility of developed ZAB can offer a potential for portable and wearable electronic applications. The robust performance under repeated bending and continuous cycling indicates that the developed catalyst and electrode design are highly suitable for next-generation flexible energy devices.

Acknowledgement

The authors acknowledge MHRD for the financial aid and Advanced Material Research Centre (AMRC), IIT Mandi for providing user facilities. A.R. and T.D. would like to acknowledge Harish-Chandra Research Institute (HRI), Prayagraj, for the infrastructure. Computational work for this study was carried out at the cluster computing facility at HRI Allahabad (http://www.hri.res.in/cluster). TD would like to acknowledge DST INSPIRE for Funding.

Declaration

This article is licensed under a Creative Commons Attribution-NonCommercial 3.0 Unported Licence

Open Access Article. Published on 18 Tachwedd 2025. Downloaded on 19/11/2025 05:45:50.

The authors used ChatGPT to check grammar, spelling, and improve readability and language.

Conflict of Interest

The authors share no conflicts of interests.

References

- Liu, Y.; Zhou, L.; Liu, S.; Li, S.; Zhou, J.; Li, X.; Chen, X.; Sun, K.; Li, B.; Jiang, J., Fe, N-Inducing Interfacial Electron Redistribution in NiCo Spinel on Biomass-Derived Carbon for Bi-Functional Oxygen Conversion. *Angewandte Chemie* **2024,** *136* (16), e202319983.
- Kumar, S.; Kumar, R.; Goyal, N.; Parida, S. K.; Anshu, A.; Yadav, A.; Yan, F.; Sahoo, B., Carbon 2. nanostructures embedded with bimetallic CoRu alloy nanoparticles as oxygen reduction electrode for zinc-air batteries. Journal of Materials Chemistry A 2025, 13 (14), 9992-10005.
- 3. Li, Z.; Ji, S.; Xu, C.; Leng, L.; Liu, H.; Horton, J. H.; Du, L.; Gao, J.; He, C.; Qi, X., Engineering the electronic structure of single-atom iron sites with boosted oxygen bifunctional activity for zinc-air batteries. Advanced Materials 2023, 35 (9), 2209644.
- 4. Fu, J.; Cano, Z. P.; Park, M. G.; Yu, A.; Fowler, M.; Chen, Z., Electrically rechargeable zinc-air batteries: progress, challenges, and perspectives. Advanced materials 2017, 29 (7), 1604685.
- Qian, J.; Liu, X.; Zhong, C.; Xu, G.; Li, H.; Zhou, W.; You, B.; Wang, F.; Gao, D.; Chao, D., Enhanced stability and narrowed D-band gap of Ce-doped Co3O4 for rechargeable aqueous Zn-air battery. Advanced Functional Materials **2023**, 33 (9), 2212021.
- Huang, H.; Liang, Q.; Guo, H.; Wang, Z.; Yan, G.; Wu, F.; Wang, J., Spray pyrolysis regulated FeCo alloy anchoring on nitrogen-doped carbon hollow spheres boost the performance of zinc-air batteries. Small 2024, 20 (23), 2310318.
- Chen, L.; Cui, L. L.; Wang, Z.; He, X.; Zhang, W.; Asefa, T., Co8FeS8/N, S-doped carbons derived from Fe-Co/S-bridged polyphthalocyanine: efficient dual-function air-electrode catalysts for rechargeable Zn-air batteries. ACS sustainable chemistry & engineering 2020, 8 (35), 13147-13158.

- 8. Hu, T.; Jiang, Z.; Fu, Z.; Jiang, Z.-J., A NiFe/NiSe 2 heterojunction bifunctional catalyst rich in oxygen vacancies introduced using dielectric barrier discharge plasma for liquid and flexible all-solid-state rechargeable Zn–air batteries. *Journal of Materials Chemistry A* **2022**, *10* (16), 8739-8750.
- 9. Chen, X.; Zhou, Z.; Karahan, H. E.; Shao, Q.; Wei, L.; Chen, Y., Recent advances in materials and design of electrochemically rechargeable zinc—air batteries. *Small* **2018**, *14* (44), 1801929.
- 10. Zhang, Y.; Wang, J.; Alfred, M.; Lv, P.; Huang, F.; Cai, Y.; Qiao, H.; Wei, Q., Recent advances of micro-nanofiber materials for rechargeable zinc-air batteries. *Energy Storage Materials* **2022**, *51*, 181-211.
- 11. Zhu, X.; Hu, C.; Amal, R.; Dai, L.; Lu, X., Heteroatom-doped carbon catalysts for zinc—air batteries: progress, mechanism, and opportunities. *Energy & environmental science* **2020**, *13* (12), 4536-4563.
- 12. Yu, T.; Zhang, Y.; Hu, Y.; Hu, K.; Lin, X.; Xie, G.; Liu, X.; Reddy, K. M.; Ito, Y.; Qiu, H.-J., Twelve-component free-standing nanoporous high-entropy alloys for multifunctional electrocatalysis. *ACS Materials Letters* **2021**, *4* (1), 181-189.
- 13. Deng, N.; Wang, Y.; Zeng, Q.; Feng, Y.; Wang, G.; Chi, H.; Kang, W.; Cheng, B., Facile construction of hierarchically porous carbon nanofibers modified by an FeCu/FeF 3 heterojunction for oxygen electrocatalysis in liquid and flexible Zn–air batteries. *Journal of Materials Chemistry A* **2025**, *13* (2), 1485-1498.
- 14. Singh, A.; Sharma, R.; Gautam, A.; Kumar, B.; Mittal, S.; Halder, A., Chemistry in rechargeable zinc-air battery: a mechanistic overview. *Catalysis Today* **2025**, *445*, 115108.
- 15. Chen, M.; Guan, J., Structural Regulation Strategies of Atomic Cobalt Catalysts for Oxygen Electrocatalysis. *Advanced Functional Materials* **2025**, 2423552.
- 16. Kundu, A.; Kuila, T.; Murmu, N. C.; Samanta, P.; Das, S., Metal–organic framework-derived advanced oxygen electrocatalysts as air-cathodes for Zn–air batteries: recent trends and future perspectives. *Materials Horizons* **2023**, *10* (3), 745-787.
- 17. Zhang, J.; Tao, H. B.; Kuang, M.; Yang, H. B.; Cai, W.; Yan, Q.; Mao, Q.; Liu, B., Advances in thermodynamic-kinetic model for analyzing the oxygen evolution reaction. *Acs Catalysis* **2020**, *10* (15), 8597-8610.
- 18. Nazir, G.; Rehman, A.; Lee, J.-H.; Kim, C.-H.; Gautam, J.; Heo, K.; Hussain, S.; Ikram, M.; AlObaid, A. A.; Lee, S.-Y., A review of rechargeable zinc—air batteries: Recent progress and future perspectives. *Nano-Micro Letters* **2024**, *16* (1), 138.
- 19. Ren, S.; Duan, X.; Liang, S.; Zhang, M.; Zheng, H., Bifunctional electrocatalysts for Zn–air batteries: recent developments and future perspectives. *Journal of Materials Chemistry A* **2020**, *8* (13), 6144-6182.
- 20. Lee, S.; Choi, J.; Kim, M.; Park, J.; Park, M.; Cho, J., Material design and surface chemistry for advanced rechargeable zinc–air batteries. *Chemical Science* **2022**, *13* (21), 6159-6180.
- 21. Chang, J.; Wang, G.; Yang, Y., Recent advances in electrode design for rechargeable zinc—air batteries. *Small Science* **2021**, *1* (10), 2100044.
- 22. Liu, X.; Zhu, Y.; Du, C.; Tian, J.; Yang, L.; Yao, X.; Wang, Z.; Ma, X.; Hou, J.; Cao, C., Cationic Codoping in copper sulfide nanosheet cathodes for efficient magnesium storage. *Chemical Engineering Journal* **2023**, *463*, 142433.
- 23. Zhang, Y.; Tao, L.; Xie, C.; Wang, D.; Zou, Y.; Chen, R.; Wang, Y.; Jia, C.; Wang, S., Defect engineering on electrode materials for rechargeable batteries. *Advanced Materials* **2020**, *32* (7), 1905923.
- 24. Qin, Y.; Lu, G.; Yang, F.; Xu, C.; Jiang, S.; Wang, Y.; Tang, Y.; Wang, P., Heteroatom-doped transition metal hydroxides in energy storage and conversion: a review. *Materials Advances* **2023**, *4* (5), 1226-1248.
- 25. Chauhan, M.; Reddy, K. P.; Gopinath, C. S.; Deka, S., Copper cobalt sulfide nanosheets realizing a promising electrocatalytic oxygen evolution reaction. *Acs Catalysis* **2017**, *7* (9), 5871-5879.

- 26. Yan, L.; Xie, B.; Yang, C.; Wang, Y.; Ning, J.; Zhong, Y.; Hu, Y., Engineering self-supported hydrophobic—aerophilic air cathode with CoS/Fe3S4 nanoparticles embedded in S, N Co-doped carbon plate arrays for long-life rechargeable Zn—air batteries. *Advanced Energy Materials* **2023**, *13* (10), 2204245.
- 27. Fu, G.; Wang, J.; Chen, Y.; Liu, Y.; Tang, Y.; Goodenough, J. B.; Lee, J. M., Exploring indium-based ternary thiospinel as conceivable high-potential air-cathode for rechargeable Zn–Air batteries. *Advanced Energy Materials* **2018**, *8* (31), 1802263.
- 28. Fu, G.; Wang, Y.; Tang, Y.; Zhou, K.; Goodenough, J. B.; Lee, J.-M., Superior oxygen electrocatalysis on nickel indium thiospinels for rechargeable Zn–air batteries. *ACS Materials Letters* **2019**, *1* (1), 123-131.
- 29. Nie, L.; Wang, H.; Chai, Y.; Liu, S.; Yuan, R., In situ formation of flower-like CuCo₂S₄ nanosheets/graphene composites with enhanced lithium storage properties. **2016**.
- 30. Liu, S.; Zhang, B.; Cao, Y.; Wang, H.; Zhang, Y.; Zhang, S.; Li, Y.; Gong, H.; Liu, S.; Yang, Z., Understanding the effect of nickel doping in cobalt spinel oxides on regulating spin state to promote the performance of the oxygen reduction reaction and zinc–air batteries. *ACS Energy Letters* **2022**, *8* (1), 159-168.
- 31. Nørskov, J. K.; Bligaard, T.; Logadottir, A.; Kitchin, J.; Chen, J. G.; Pandelov, S.; Stimming, U., Trends in the exchange current for hydrogen evolution. *Journal of The Electrochemical Society* **2005**, *152* (3), J23.

Open Access Article. Published on 18 Tachwedd 2025. Downloaded on 19/11/2025 05:45:50.

Price Access Article is licensed under a Creative Commons Attribution-NonCommercial 3.0 Unported Licence.

Data availability: The additional data supporting this article have been included as part of the AO7350B ESI.